

A Behavior-Learned Cross-Reactive Sensor Matrix for Intelligent Skin Perception

Jun Ho Lee, Jae Sang Heo, Yoon-Jeong Kim, Jimi Eom, Hong Jun Jung, Jong-Woong Kim, Insoo Kim, Ho-Hyun Park, Hyun Sun Mo,* Yong-Hoon Kim,* and Sung Kyu Park*

Mimicking human skin sensation such as spontaneous multimodal perception and identification/discrimination of intermixed stimuli is severely hindered by the difficulty of efficient integration of complex cutaneous receptor-emulating circuitry and the lack of an appropriate protocol to discern the intermixed signals. Here, a highly stretchable cross-reactive sensor matrix is demonstrated, which can detect, classify, and discriminate various intermixed tactile and thermal stimuli using a machine-learning approach. Particularly, the multimodal perception ability is achieved by utilizing a learning algorithm based on the bag-of-words (BoW) model, where, by learning and recognizing the stimulus-dependent 2D output image patterns, the discrimination of each stimulus in various multimodal stimuli environments is possible. In addition, the single sensor device integrated in the cross-reactive sensor matrix exhibits multimodal detection of strain, flexion, pressure, and temperature. It is hoped that his proof-of-concept device with machine-learning-based approach will provide a versatile route to simplify the electronic skin systems with reduced architecture complexity and adaptability to various environments beyond the limitation of conventional “lock and key” approaches.

Recently, the realization of artificial sensory systems mimicking the biological perception has been intensively pursued for the next generation neuromorphic electronics and humanoid robots. Particularly, an artificial somatosensory system which can emulate the functions of the biological skin and body sensation is considered to have a great potential in achieving highly integrated and neuromorphic sensory network. The biological somatosensory system is a complex sensory network, which is composed of sensory neurons (receptors), neural pathways, and a part of the brain for the perception process. By the sensory receptors such as mechanoreceptors, thermoreceptors, and nociceptors,^[1–10] which are located on or beneath the skin, various environmental stimuli are detected and transmitted to the brain through the neural pathways. This enables the specific sensations such as strain, pressure, temperature, and distortion (flexion/bending) of the body. In realizing an artificial somatosensory system, however, the integration of a large amount of sensory networks for the individual sensation still remains as a significant challenge, especially in the case of large-area electronic skin (e-skin) devices. For example, it is reported that to realize an e-skin for robotics and prosthetic limbs, an estimated 45 000 mechanoreceptors are needed in about 1.5 m²-area devices.^[11] Additionally, the number of sensors could increase even further, considering the e-skins to have equivalent numbers of thermoreceptors and nociceptors in the system. Therefore, to fully mimic the biological skin perception over a large-area, a large number of sensory systems with complicated multi-layer architectures would be required as well as a large amount of data associated with their perception processing.

In recent research, a new strategy to achieve artificially intelligent perception has been introduced in chemical and gas detection systems by analyzing the different responses recognized from many cross interferences.^[12–18] These cross-reactive sensory systems, inspired by mammalian olfactory and gustatory systems, can simultaneously detect and identify specific responses from a variety of non-specific vapor, liquid elements, and their combinations by analyzing the difference in sensing responses with pattern recognition and machine learning algorithms.^[19–27] Although these previous advances are noteworthy,

J. H. Lee, Dr. J. S. Heo, Y.-J. Kim, Prof. H.-H. Park, Prof. S. K. Park
School of Electrical and Electronics Engineering
Chung-Ang University
Seoul 06980, Korea
E-mail: skpark@cau.ac.kr

Dr. J. S. Heo, Prof. I. Kim
Department of Medicine
University of Connecticut School of Medicine
Farmington, CT 06030, USA

Dr. J. Eom, Prof. Y.-H. Kim
School of Advanced Materials Science and Engineering
Sungkyunkwan University
Suwon 16419, Korea
E-mail: yhkim76@skku.edu

H. J. Jung, Prof. H. S. Mo
School of Electrical Engineering
Kookmin University
Seoul 02707, Korea
E-mail: tyche@kookmin.ac.kr

Prof. J.-W. Kim
School of Advanced Materials Engineering
Chonbuk National University
Deokjin-Dong, 664-14, Jeonju 54896, Korea

 The ORCID identification number(s) for the author(s) of this article can be found under <https://doi.org/10.1002/adma.202000969>.

DOI: 10.1002/adma.202000969

it is still rather problematic to fully translate the cross-reactive system into artificially perceptive electronics at this initial stage, possibly due to the lack of facile device architectures and appropriate protocols. More importantly, since most of the current e-skin technologies are essentially based on “lock and key” approaches, the numeric data signals measured from the superposed stimuli could not be cross-operated with each other, leaving the difficulty of decoupling interference of intermixed signals and of integrating cross interferences for recognizing the behavior of each stimulus.^[28–32] To address these issues, in a previous work, a field-effect transistor composed of a piezo-pyroelectric gate dielectric and a piezo-thermorestive organic semiconductor channel was utilized, showing the simultaneous response to two stimuli of pressure (or strain) and temperature. However, this approach is only available for a limited range of deformability, resulting in a restricted range for practical applications.^[33] Consequently, a new strategy capable of providing substantial advances for the state-of-the-art e-skin technology is required for discriminating and classifying intermixed signals composed of known and unknown stimuli.

Here, we explore a highly stretchable cross-reactive sensor matrix with artificial perception technology to detect, classify, and discriminate various intermixed tactile and thermal stimuli based on machine learning. The 10×10 stretchable cross-reactive sensor matrix is composed of cross-aligned highly stretchable electrodes and multimodal hybrid sensing elements sandwiched between the electrodes, exhibiting high sensitivities and fast responses to diverse stimuli such as strain, pressure, flexion, and temperature with a cross-operated manner. Moreover, the multimodal perception is achieved by utilizing a machine learning algorithm, based on the bag-of-words (BoW) model, discriminating each stimulus by recognizing distinct 2D image patterns generated by the intermixed tactile and thermal stimuli. This design strategy of cross-reactive sensor matrix allows the construction of distinctive areal pattern data, providing the basis for BoW-based machine learning process to identify each stimulus. Accordingly, with using such strategy, the discrimination of a specific or even unknown stimulus is possible by decoupling the intermingled tactile and thermal stimuli. The results reported here imply that the cross-reactive sensor matrix operated with machine learning algorithm would offer a facile route to realize high-performance and reliable artificial e-skin with marginal complexity and compatibility with large-scaled applications such as wearable health monitoring systems, electronic prosthetics, and smart robotics.

Figure 1a schematically illustrates the structure of cross-reactive sensor device and a 10×10 array (see Experimental Section and Figure S1, Supporting Information, for detailed fabrication procedures). Cross-aligned highly stretchable silver nanowire-coated polyurethane (AgNW/PU) fibers (electrical conductivity of $\approx 56.87 \text{ S cm}^{-1}$) are placed with carbon black (CB)-dispersed poly(dimethylsiloxane) (C-PDMS) sandwiched between them as a multimodal sensing element. To maintain the device structure from the external stimuli such as strain, PDMS molding was carried out over the entire sensor matrix. The electrical conductance of C-PDMS is designed to easily respond to various tactile and thermal stimuli, while that of the stretchable electrodes (AgNW/PU) with pre-strained coating is almost insensi-

tive to these stimuli (Figure S2, Supporting Information). In the C-PDMS, CB nanoparticles are uniformly distributed in the PDMS matrix (Figure S3, Supporting Information). At initial state, without any stimulus applied, the sensor delivers a current of $\approx 0.2 \mu\text{A}$ at 0.1 V (an average contact resistance of 100 pixels is $51.43 \text{ k}\Omega \pm 0.34$, Figure S4, Supporting Information), and the conductivity tends to vary with the intensity of stimulus applied to the sensor (Figure 1b). As shown in Figure 1c, two main physical changes of CB nanoparticles are expected to occur in the C-PDMS matrix by the external stimuli. At first, when the sensor is deformed by stretching or bending, the transverse compressive force leads to the displacement of CB nanoparticles in the PDMS matrix, resulting in more intimate contacts between the CB nanoparticles and an increase of conductive pathways within the matrix. When the intensity of the applied stimulus is increased, the thickness of C-PDMS is further reduced, creating additional conductive pathways resulting in a large decrease in resistance. The cross-reactive sensor is also sensitive to temperature variation. Due to a large difference in the thermal expansion coefficients (CTEs) of CB nanoparticles ($3\text{--}4 \times 10^{-6} \text{ K}^{-1}$) and the PDMS matrix ($9 \times 10^{-4} \text{ K}^{-1}$), the distances between the CB nanoparticles are extended when the temperature is increased, causing an increase of resistance (Figure S5, Supporting Information). Since the cross-reactive sensor device is composed of all elastic substances, the vice versa characteristics are well reproduced in all cases.

Prior to the investigation on the cross-reactive sensing behavior in an array platform, the static and dynamic responses to various stimuli such as strain, pressure, flexion, and temperature were evaluated as shown in **Figure 2**. Here, the sensing performance is characterized by measuring the relative change of current under different stimulus (Note S1, Supporting Information). For the strain stimulus ranging from 0 to 40%, the sensor exhibits relatively high sensitivity (gauge factors (GFs) of 81.2 and 28.5 in the strain ranges of 0–5% and 5–40%, respectively) and good repeatability with a fast response time of less than 50 ms in all ranges. The different GFs in the two regions are attributed to the transition in the main conductive paths of CB nanoparticles corresponding to the stimulus intensity as described above, relating to Figure 1c (see also Figure S6, Supporting Information). In addition, the response of the sensor was reasonably stable without any noticeable degradation during 4000 cyclic stretching and releasing test and dynamic cyclic test in diagonal direction indicating that the sensor has good durability (Figure S7, Supporting Information). Figure 2c,d shows the static and dynamic responses to the pressure with fast response and short relaxation times. The average response and relaxation time are around 100 and 110 ms with minimum values of around 80 and 60 ms, respectively (Figure S8, Supporting Information), which are comparable to those of recent tactile sensors (Table S1, Supporting Information). We also evaluated the sensing behavior to flexion by varying the bending angle from 0° to 150° (Note S2, Supporting Information). As shown in Figure 2e,f, the cross-reactive sensor showed a significant change in current at angles between 60° to 90° .

Meanwhile, in smaller angle ranges, the devices show a small amount of current changes. It indicates that the change of small angle below 60° is still not enough to be precisely

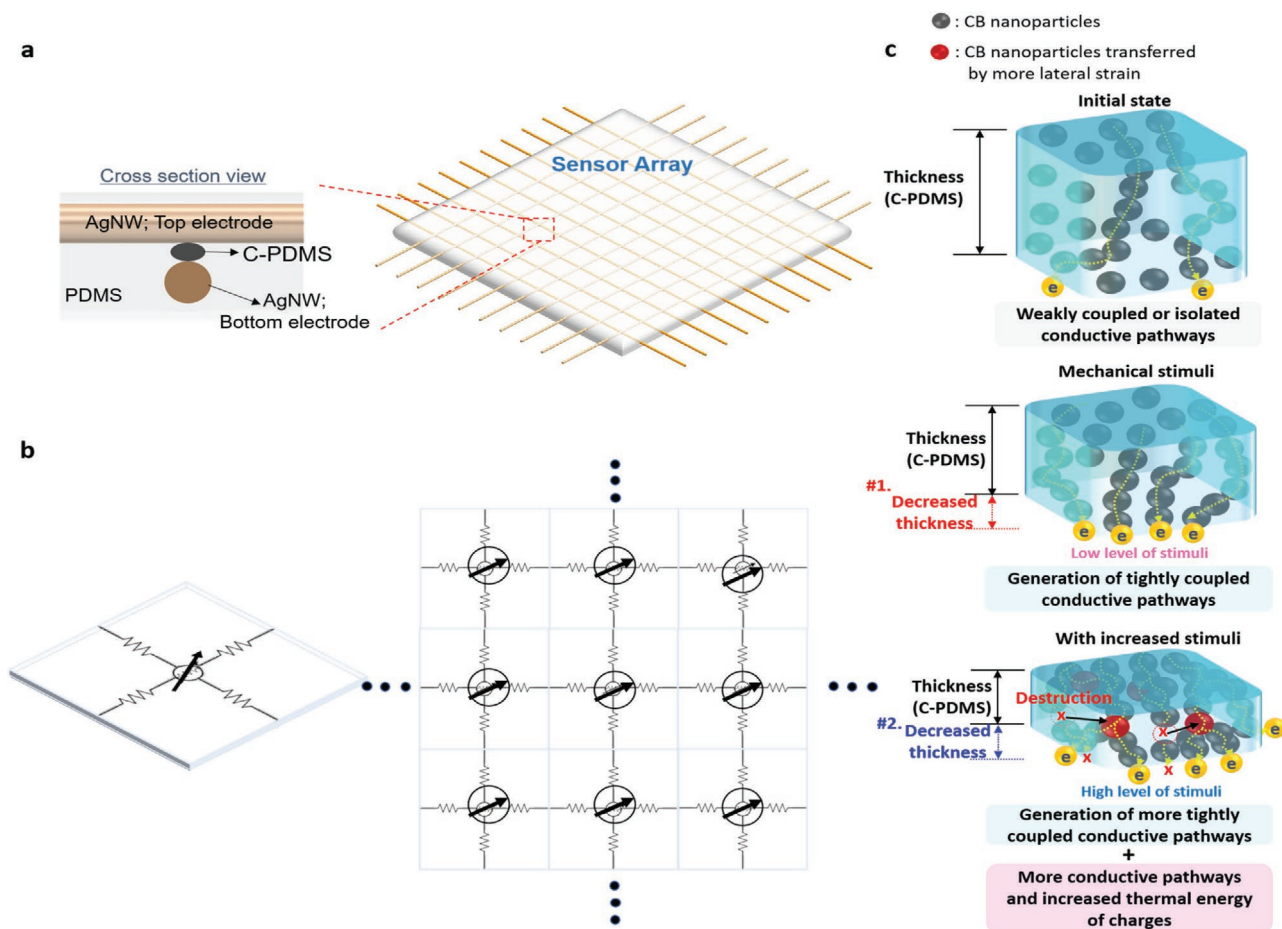


Figure 1. The structure of cross-reactive sensor device/array and the sensing mechanism. a) The structure of a cross-reactive sensor unit and a 10×10 sensor matrix. The sensor comprises of two cross-aligned stretchable silver nanowire (AgNW)-coated polyurethane (PU) fibers as top and bottom electrodes, carbon black (CB)-dispersed poly(dimethylsiloxane) (C-PDMS) as a multimodal sensing element, and PDMS molding. b) A schematic diagram of cross-reactive sensor unit and the array. c) The sensing mechanism of cross-reactive sensor unit. The thickness of C-PDMS and the displacement of CB nanoparticles in the PDMS matrix are varied according to the intensity of the stimuli.

detected. It is speculated that to improve the sensitivity to small angle flexion, more strain-sensitive materials along with the modification of sensor structure may be required for more diverse applications. Further to expand the scope of cross-reactivity of the sensor, the response characteristics for thermal stimulus were also investigated. As shown in Figure 2g, the current decreases with the temperature, attributing to the large difference in the CTEs of PDMS and CB nanoparticles. The change of resistance with temperature exhibits a linear-like relationship in the temperature range of 25–150 °C, corresponding to a temperature coefficient resistance of 0.515 ppm K^{-1} . Furthermore, to evaluate the dynamic response characteristics for temperature, a temperature cycling test was carried out as shown in Figure 2h. The sensor showed a response time of ≈ 8.4 s which is relatively longer than those of carbon-based temperature sensors.^[26,34] However, although the sensing response is relatively slow, the wider range of temperature sensing may extend its utilization in practical applications (Table S1, Supporting Information).

Due to the multimodal sensing capability of the cross-reactive sensor device, the output signal typically contains

information from various stimuli when exposed to a complex environment. For example, as shown in Figure S9, Supporting Information, the response to strain and pressure may change according to the ambient temperature. This conversely states that when an appropriate perception method is applied, it can be possible to determine both the temperature and strain (or pressure) simultaneously. Prior to applying a machine learning model for the artificial skin perception, we examined the specific response behavior to each stimulus to evaluate the fidelity of such model. To pose the stringencies on the quality of the information produced by the device, monolithically arrayed 2D architecture is implemented, and thereby, every node reacts to a specific stimulus, exhibiting corresponding areal-pattern and areal-gradation of output signals. Such a geometry and/or strength profile of output signals would thus provide unique opportunities to discriminate various stimuli applied to the device.

To characterize specific response behaviors, the $\Delta I/I_0$ values at each node of the cross-reactive sensor matrix were analyzed and spatially recorded across 100 node points (10×10 matrix). The cross-reactive sensor arrays exhibited different physical

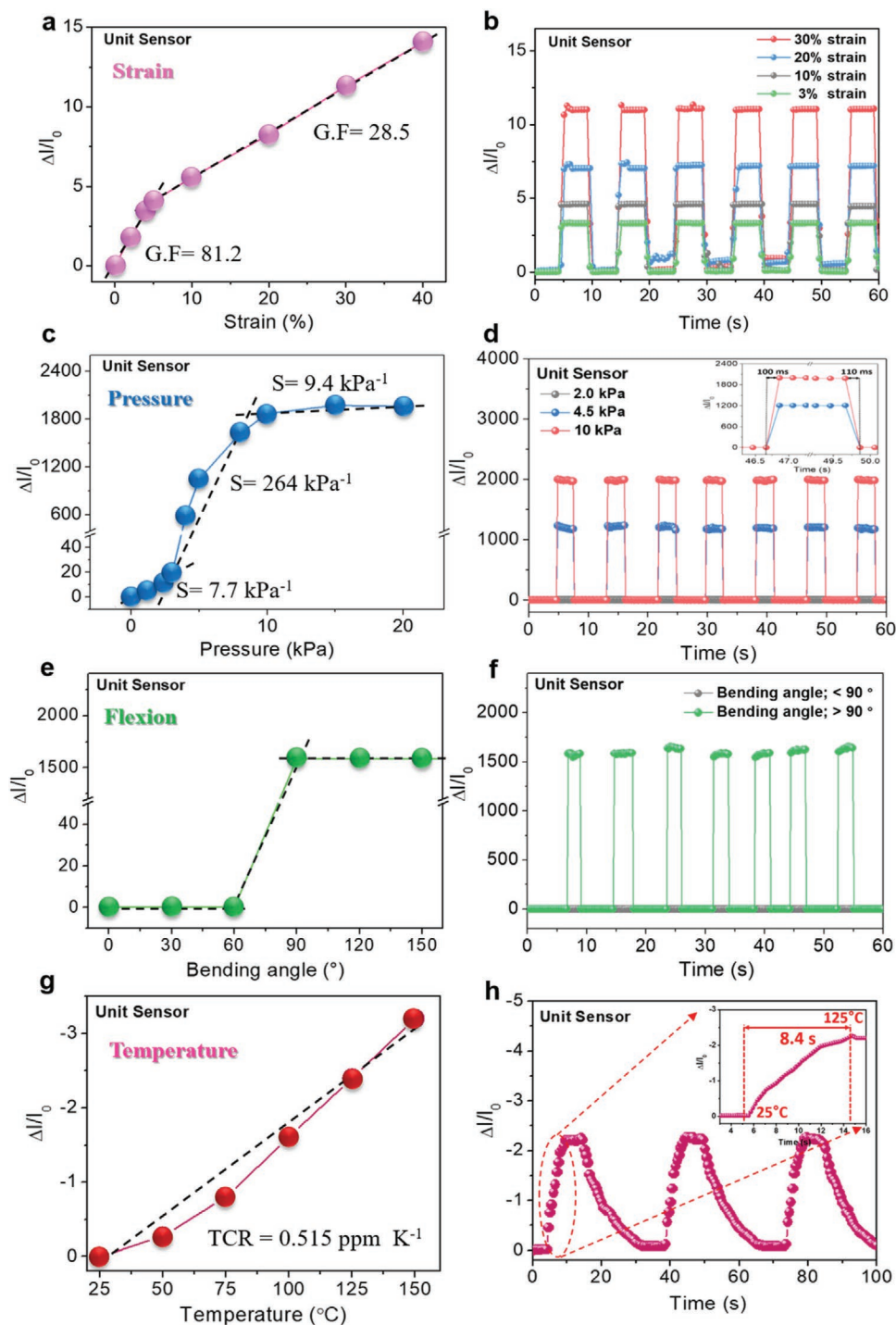


Figure 2. Analysis of static and dynamic responses to individual stimulus. a) The relative change in current ($\Delta I/I_0$) as a function of strain in the range of 0–40%. In the strain range of 0–5% and 5–40%, the corresponding gauge factors were 81.2 and 28.5, respectively. b) A dynamic response to strain cycles ranging from 0 to 30%. c) The relative change in current as a function of pressure in the range of 0–20 kPa. d) A dynamic response to pressure cycles ranging from 2.0 to 10 kPa. The inset shows the response time (≈ 100 ms) and the relaxation time (≈ 110 ms) from 0 to 4.5 and 10 kPa. e) The relative change in current as a function of flexion in the range of 0–150°. f) A dynamic response to flexion cycles ranging from 0 to 90°. g) The relative change in current as a function of temperature in the range of 0–150 °C (temperature coefficient of resistance of 0.515 ppm K⁻¹). h) A dynamic response to temperature cycles ranging from 25 to 125 °C. The inset shows the rising time (≈ 8.4 s) from 25 to 125 °C.

and structural sensing resolutions for the recognition of each stimulus in an array platform (Table S2, Supporting Information). The physical resolution of the sensor array is supposed

to be further enhanced by adopting more sensitive materials and increasing the density of sensors in the array. The sensor matrix is fully addressable and readable from external com-

ponents, allowing the acquisition of the position-dependent data at a high rate. At first, single strain, pressure, flexion, or temperature stimulus was applied to the sensor matrix and its specific response was examined by 2D areal mapping, which is verified by comparing the experimental data with the theoretical data obtained from finite-element analyses (FEA) simulation. The details for the numerical modeling are described in the Experimental Section and Note S3, Supporting Information. As shown in **Figure 3a**, when a strain is applied along one axis, a gradual and wide-range increase of current was observed in the node points along the strained direction. Here, the gradation weight value ($W_{x,y}$), which is defined as the ratio of current increase between the adjacent nodes is defined by Equation (1):

$$W_{x,y} = (I_{[n+1,y]} - I_{[n,y]}) / I_{[n,y]} \quad (1)$$

where x and y are the row and the column number in the matrix, respectively. In the case of strain applied to the upper part of the matrix, the gradation values were observed 3%, 5%, and 7% for regions I, II, and III (**Figure 3c**), respectively in overall device (**Figure 3b–d**; **Figure S10**, Supporting Information). On the other hand, when applying a flexion force, an abrupt increase of $\Delta I/I_0$ and gradation value were observed (0%, 0.65%, and $>10^4\%$ for angles of 30° , 60° , and 90° , respectively), exhibiting a narrow and large gradation region only near the flexion axis (**Figure 3e–h**). Similarly, for a pressure, a sharp increase of $\Delta I/I_0$ was exhibited on the pressed area as well as their corresponding pressure gradation distributions, as like an

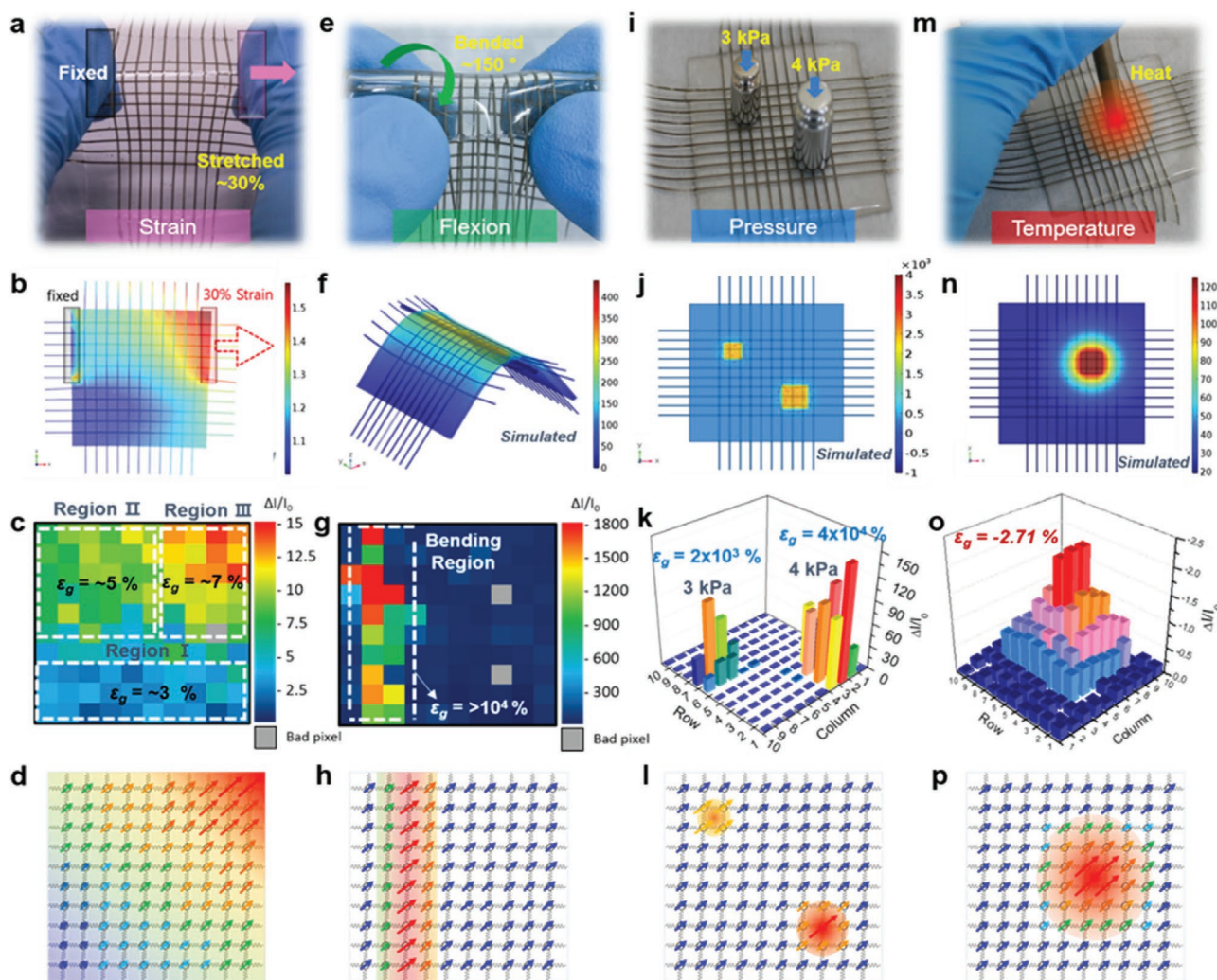


Figure 3. Analysis of specific response behaviors to tactile and thermal stimuli. a) A photograph of 30% stretched cross-reactive sensor matrix. b,c) Corresponding 2D strain distribution data from simulation by finite-element analysis (FEA) (b) and experimental measurement (c). The gradation values were 3%, 5%, and 7% for regions I, II, and III, respectively. e) A photograph of 150° -bent cross-reactive sensor matrix (flexion). f,g) Corresponding 2D flexion distribution data from simulation by FEA (f) and experimental measurement (g). The gradation values were 0%, 0.65%, and $>10^4\%$ for angles of 30° , 60° and 90° , respectively. i) A cross-reactive sensor matrix with two objects having weights (3 and 4 kPa). j,k) Corresponding pressure distribution data from simulation by FEA (j) and experimental measurement (k). The gradation values were $2 \times 10^3\%$ and $4 \times 10^4\%$ for 3 and 4 kPa, respectively. m) A photograph of cross-reactive sensor matrix with a heat stick. n,o) Corresponding temperature distribution data from simulation by FEA (n) and experimental measurement (o). The gradation values -2.71% . d,h,l,p) Schematic diagrams of corresponding 2D spatial data for strain, flexion, pressure, and temperature, respectively.

island-like geometry, which corresponds to the weight and the pressed area (Figure 3i–l). In addition, the gradation values of $2 \times 10^3\%$ and $4 \times 10^4\%$ were exhibited for 3 and 4 kPa respectively. In addition to the tactile deformations, for the temperature sensing, the spatial and gradient distributions of $\Delta I/I_0$ are measured with a heating stick placed ≈ 5 mm above the sensor surface (Figure 3m), to avoid any intermixing with other stimuli such as pressure. As shown in Figure 3n–p, the sensor matrix showed a radial-shaped gradation distribution which increased outward from the central point contrary to those of the pressure stimulus. The gradation value at the heated area depends on the temperature such that 0%, -1.92% , and -2.71% for 25, 100, and 125 °C, respectively. Consequently, the experimental and simulation results indicate that the strain affects the whole array region with rather low gradation values, while the pressure and flexion affect only localized regions with high gradation values. Especially, it might be discriminated from the two stimuli of pressure and flexion because the gradation produced by flexion is higher than that by the pressure. Moreover, the response behavior of thermal stimulus shows a negative radial gradation conversely compared to the other tactile stimuli. Therefore, the discrimination of temperature stimulus from

other tactile stimuli can obviously be available. According to the results above, it is supposed that the multimodal perception of the cross-reactive sensor matrix would be achieved by recognizing distinct responsive behaviors based on the areal distributions of $\Delta I/I_0$ or the gradation values acquired from different stimuli.

Aforementioned, the cross-reactive sensor matrix would be capable of detecting multiple stimuli, simultaneously. Moreover, since the $\Delta I/I_0$ data obtained from the 100 node points can be considered as a 10×10 pixel image, containing the information of intermixed stimuli, it is possible to use the conventional image analysis methods in analyzing the data. For discriminative detection of superposed stimuli, we first evaluated the feasibility of using the edge-detection algorithm (EDA) method as shown in Figure 4. The EDA process has been often used to find spatial behaviors such as boundary (edge) detection of data array in neural network and image processing fields.^[35] Thus, we suggested that since the cross-reactive sensor matrix exhibits unique spatial behaviors for each stimulus, the EDA could be utilized to distinguish and isolate the specific signals by using the boundary recognition (edge detection). Here, the Sobel EDA with two 3×3 convolution masks was used, which

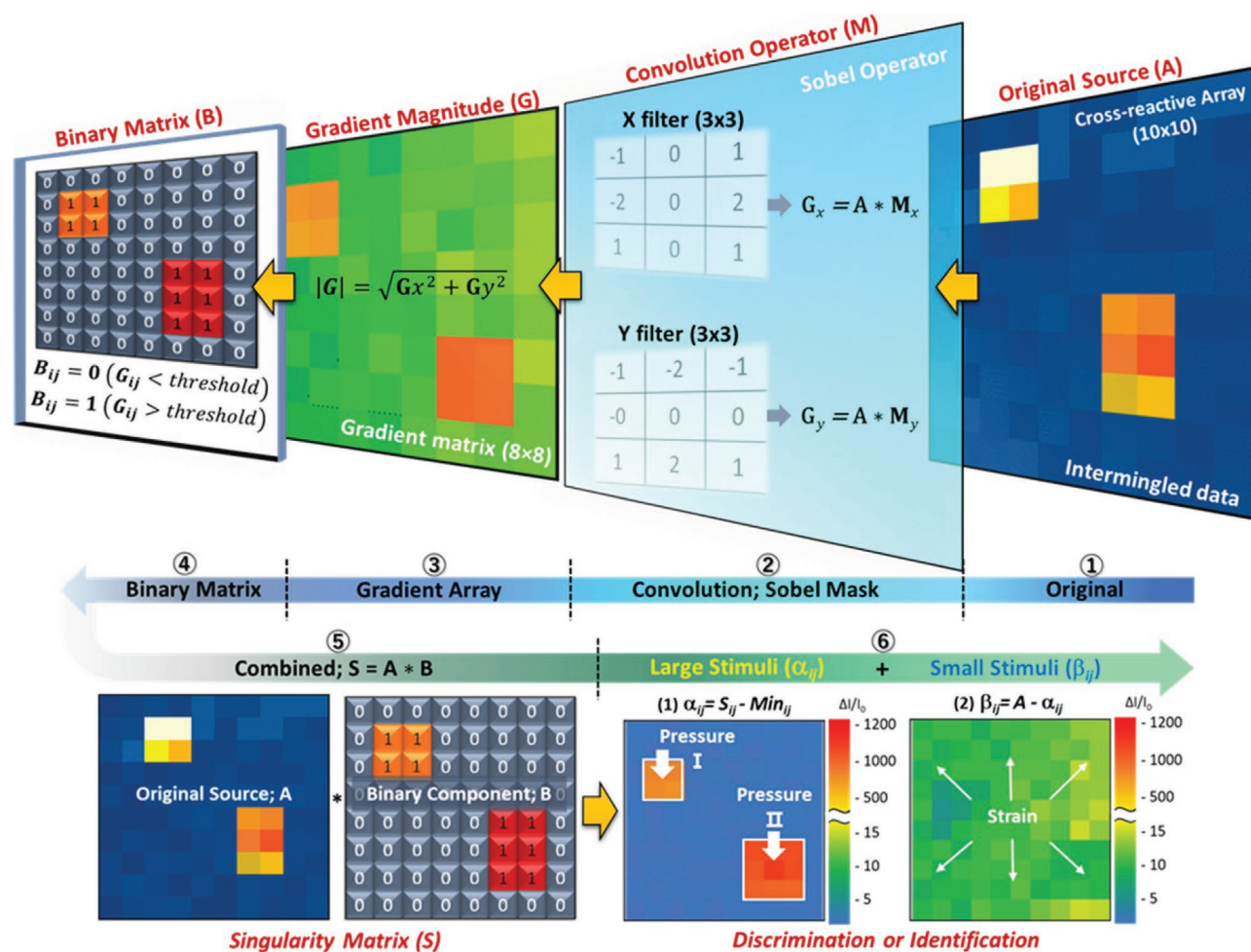


Figure 4. The edge-detection algorithm (EDA) process for multimodal and discriminable skin perception. Schematics showing the discrimination procedure using the EDA method for intermixed stimuli. For the discrimination of intermixed stimuli, a Sobel mask, gradient, binary, singularity, and discrimination for large and small stimuli were carried out.

are superposed with the sensing data array to calculate approximations of the derivatives; one mask (X filter) identifies the horizontal gradation and the other mask (Y filter) identifies the vertical gradation. To calculate a gradation value for a specific pixel with its vicinity 8 pixels (G , gradient magnitude), the convolution operation mask M is convolved with a matrix A , where M and A are defined as a 3×3 convolution mask and as an original source data (intermixed data of stimuli α and β), respectively. As a result, G_x and G_y are two reproduced data which contain the horizontally and vertically orientated gradation, respectively. Here, G denotes the criterion value for defining the specific stimulus, which has been obtained from the experimental data for individual stimulus. Moreover, binary matrix B (8×8) made by G values is combined with original source data A . The detailed procedures for obtaining the G values and the Sobel masking process are described in Note S4, Supporting Information.

To validate the simultaneous detection of various intermixed stimuli using the cross-reactive sensor matrix and the EDA process, we examined the response behaviors to several intermixed stimuli such as strain/pressure, pressure/flexion, flexion/strain, temperature/pressure, and strain/pressure/flexion combinations (Figure 5; Figure S11, Supporting Information). For the criterion of our results, the G values are 8–10 for the strain range from 0% to 40%, 75 for the temperature ($RT \approx 120$ °C), >4000 for the flexion (>90°), and >250 for the pressure (0–15 kPa). Figure 5 shows that the discrimination and isolation of each tactile stimulus from the intermixed stimuli could be achieved by comparing both the G values and their specific distribution patterns as well as the gradient polarity (negative for temperature stimulus). To verify the method, we performed the decoupling process and then extracted the specific stimulus signal from various superposed stimuli signals (Figure 5; Figures S12 and S13, Supporting Information). As shown in Figure 5a, the superposed stimuli including strain (20%) and pressure (3 and 4 kPa) were applied to the sensor matrix and the discrimination process of each stimulus was carried out. First, the pressure data were isolated by extracting the large gradient data in the pressed areas and then the strain data were discriminated which have similar gradation values with adjacent nodes. The result indicates that discrete strain and pressure information can be clearly isolated using the EDA method (Figure 5a). In addition, in order to verify the result, the discriminated data were compared with the simulation data, as shown in Figures S12 and S13, Supporting Information showing the comparison for strain/pressure and pressure/temperature intermixed stimuli, respectively. For both cases, the accuracy has been tested for five times in ten devices by comparing all same position pixels of measured data with simulated data, showing that the accuracies were >95% and >94% with the every standard average deviation of 11.76 for the experiment and the simulated data respectively. The accuracy described here is calculated as the average of difference in all same coordinate pixels by comparing the data from the discriminated strain mapping and the single strain mapping data. Also, an intermixed signal of pressure (3 kPa) and flexion (>150°) was also examined using the identical procedure. The flexion was first discriminated by extracting the abruptly changed linear data and subsequently the remaining data was extracted which represents the pres-

sure applied to the sensor matrix, as shown in Figure 5b. For the flexion (>150°) and strain (20%) intermixed stimuli (Figure 5c), the flexion data not only can be extracted but also the distribution of strain can be identified using the identical process. In addition, to investigate the discriminability about the temperature (≈ 100 °C) and pressure (3 kPa) intermixed stimuli, two vials filled with hot and cold water were placed on the sensor matrix and then the pressure and temperature stimuli and their corresponding distributions were discriminated and identified, respectively, as shown in Figure 5d. The EDA method can be also applied for more complex intermixed stimuli comprising strain (20%), pressure (3 kPa), and flexion (over 150°). As shown in Figure 5e, by extracting the signals in the order of pressure, flexion, and strain, a clear mapping and identification of each stimulus was achieved, validating that the EDA-based process is an effective approach for discriminating the intermixed tactile and temperature stimuli using the cross-reactive sensor matrix. In some special cases, when the positions and the shapes of the intermixed stimuli are exactly the same (cf. pressure/flexion in lines at the same position), the discrimination would be difficult. However, we expect that these limitations can be resolved by increasing the spatial resolution of the sensor array, such as 100×100 pixel arrays.

Although the EDA method can carry out the multimodal sensation and discrimination of the intermixed stimuli, there still remain limitations such as identifying unknown stimuli and intentionally setting the thresholds for the gradient values. Therefore, in this perspective, more reliable and self-adaptable learning-based method for discrimination and identification of intermixed stimuli is definitely required. Among various machine learning algorithms developed for the categorization and pattern recognition of image data, we adopted the BoW model which is typically used in image categorization process.^[36] Figure 6 shows the process flow of discriminating the intermixed stimuli using the BoW-based machine learning algorithm. In the case of typical machine learning, the training is implemented by the data based on 1D matrix. However, in this study, we converted the $\Delta I/I_0$ data into an image of 8-bit grayscale (in the range of values from 0 to 255) using the data trained in the 10×10 matrix of cross-reactive sensor. For this process, the maximum values of the strain, pressure, flexion, temperature, and the intermixed data were normalized to 255, while the minimum values were set to 0 (the minimum current without the stimulation). As shown in Figure S14, Supporting Information, the results indicated that the stimuli applied to the cross-reactive sensor matrix could be converted into grayscale images.^[37] For the training process, a total of 360 converted data sets are used and 240 data sets are used for the verification of the algorithm. For the single stimulus, 50 data sets were prepared for each. In detail, the setting data are 0% to 40%, 0 to 15 kPa with two square shapes, with randomly distributed horizontal or vertical line over a threshold angle, RT to 150 °C with an interval of 2 or 3 °C for strain, pressure, flexion, and temperature, respectively. Also, for the intermixed stimuli, 100 different data sets were prepared for strain/pressure, pressure/temperature, strain/temperature, and strain/pressure/temperature combinations.

As shown in Figure S15, Supporting Information, to classify the images, key-points are extracted from the image using

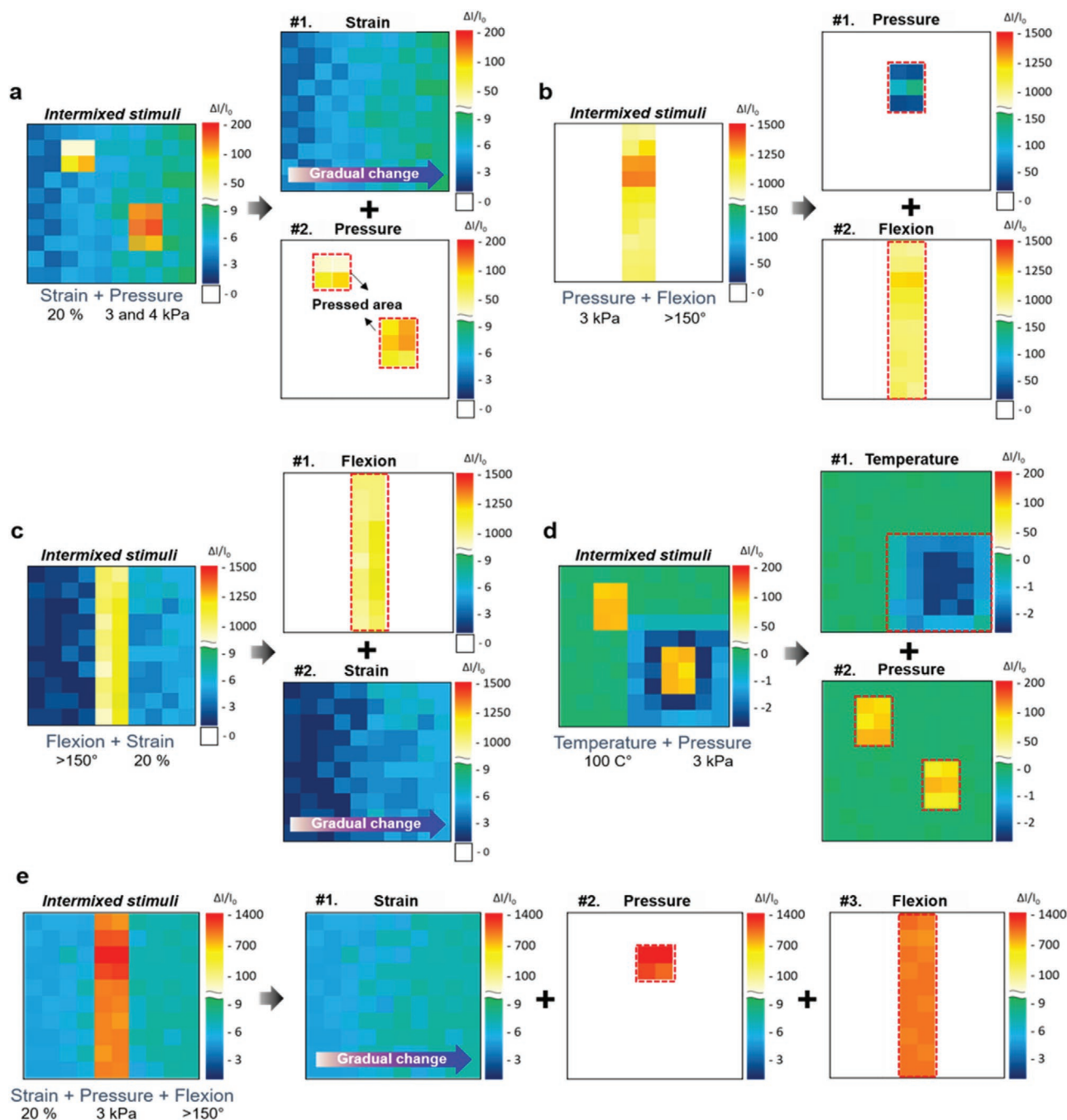


Figure 5. Discrimination of intermixed stimuli using the EDA method. Discrimination of various intermixed stimuli using the EDA method. a) Strain (20%)/pressure (3 and 4 kPa), b) pressure (3 and 4 kPa)/flexion (>150°), c) flexion (>150°)/strain (20%), d) temperature (100 °C)/pressure (3 and 4 kPa), and e) strain (20%)/pressure (3 and 4 kPa)/flexion (>150°) combinations. Using the gradient values and their specific distribution patterns and the gradient polarity, each tactile or thermal stimulus was discriminated from the intermixed stimuli.

the speeded-up robust features (SURF) algorithm.^[38] Then, through the *K*-mean clustering, any duplicated or weak keypoints are removed. Afterward, based on the representative keypoints, a codebook is created. Finally, using the codebook and the support-vector-machine (SVM) model, the encoded training images are fitted to feature vectors. After the training is completed, when a new input data set is inserted, the key features of the image are extracted and identified which stimulus cat-

egory vector is similar to the extracted key-features as shown in Figure S16, Supporting Information. Finally, an answer is given for the input data set. Figure S17, Supporting Information, shows the accuracy of identifying single and intermixed stimuli for the training and verification data sets. For the training data sets, the accuracies for identifying strain, pressure, flexion, and temperature were 98%, 96%, 90%, and 100%, respectively. For the verification data sets, the accuracies for identifying strain,

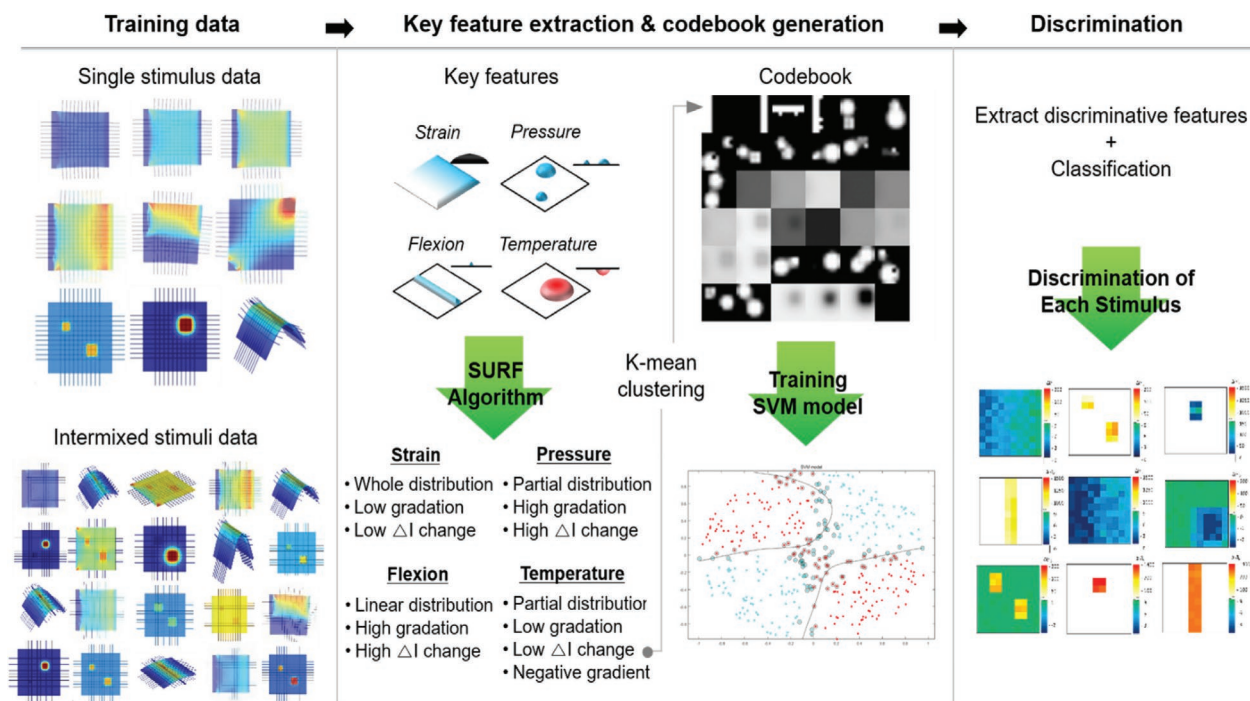


Figure 6. Discrimination of intermixed stimuli using the bag-of-words (BoW) algorithm. 2D current mapping data of single and intermixed stimuli are used for the training. The 2D current mapping data were generated by using the FEA. The key features are extracted from the image through the SURF algorithm. Afterward, K-mean clustering is performed on all of the key features extracted from the plurality of images to remove duplicate or weak key-points. Then, when a new image is input, the feature points of the image are extracted and the closest feature vector corresponding to each of the extracted key features in the codebook and the SVM is found and classified by applying the category of the feature vector.

pressure, flexion, and temperature were 97%, 98%, 90%, and 95%, respectively. In addition, for the cases of unknown intermixed stimuli of strain/temperature, pressure/temperature, and strain/pressure/temperature, the accuracies of identification were 93%, 94%, and 92% which is similar to that for the known single and intermixed stimuli (Note S5, Supporting Information). Overall, we first mimicked the multimodal skin perception that simultaneously detects and discriminates various stimuli using the cross-reactive sensor matrix and the machine learning algorithm. By adopting the BoW model-based learning algorithm to discriminate and identify the single and intermixed stimuli, accuracies over 90% were successfully achieved even with relatively small number of training process (360 sets). We believe that the machine learning-based algorithm can be extended to other superposed stimuli and also one-shot learning of unidentified stimuli, replicating the functions of biological skin perception.

The results reported here argue that the combination of a stretchable cross-reactive sensor matrix with machine learning algorithm can be a general route to realize high-performance and multimodal perception e-skin with marginal complexity, offering the compatibility with large-scaled applications such as smart health monitoring systems, perceptive electronic prosthetics, and smart robotics. Furthermore, by implementing a more delicate device architecture and design for various sensations, the strategy might allow the accuracy and sensing properties to be fine-tuned and become particularly vital when meeting application-specific needs such as biologically mimicking perceptive electronics.

Experimental Section

Fabrication of AgNW-Coated PU Fiber Electrodes and C-PDMS Composites: For the fabrication of fiber-type electrode, a PU fiber with an average diameter of 400 μm was treated with UV/ozone for 5 min to form hydrophilic surface. On the PU fiber, AgNWs (average length of 15 μm , average diameter of 30 nm, 1% isopropyl alcohol dispersion, Ditto Technology Co.) were coated by using the dip-coating method. Prior to the dip coating process, the PU fiber was first pre-stretched for 30% to enhance the mechanical stability (Figures S18 and S19, Supporting Information). Then, the AgNW-coated PU fiber was annealed at 100 $^{\circ}\text{C}$ for 10 min in an oven. This process was repeated for five times, giving an optimized thickness and conductivity with an electrical conductivity of 56.87 S cm^{-1} . The C-PDMS composite was prepared by mixing CB nanoparticles (particle size < 500 nm, Sigma Aldrich) and PDMS (Sylgard 184, Dow Corning). For PDMS, the ratio of base to curing agent was 10:1 in weight. To uniformly disperse the CB nanoparticles in PDMS matrix, the CB was first diluted in toluene, followed by a sonication for 1 h. The PDMS base materials were also diluted in toluene (a weight ratio of 1:1) and stirred for 2 h. Subsequently, both solutions were mixed together and the curing agent for PDMS was added and stirred at 80 $^{\circ}\text{C}$ for 12 h to fully evaporate the toluene. As shown in Figure S20, Supporting Information, the sensing characteristics were dependent on the CB content. 30 wt% of CB, which showed the highest sensitivity and stability against strain and pressure was used in this work. The electric conductivity of C-PDMS was 7.54 S m^{-1} which is comparable with previously reported PDMS-based conductive composites.^[39,40]

Fabrication of Fiber-Based Sensor Unit and 10 × 10 Matrix: On a carrier glass substrate, the PDMS solution was coated by spin coating. For PDMS, the ratio of base and curing agent was 10:1. Then, a soft-baking at 70 $^{\circ}\text{C}$ for 10 min was followed to form a viscose and sticky film. Next, to fabricate the sensor matrix with orthogonally aligned fibers, an AgNW-coated PU fiber (bottom electrode) was positioned on the soft-baked PDMS substrate. Subsequently, $\approx 1.25 \mu\text{L}$ of C-PDMS solution was

dropped on the bottom electrode. Finally, another AgNW-coated PU fiber (top electrode) was placed on the C-PDMS. Finally, PDMS molding was carried out to firmly hold the sensor structure and to prevent the delamination of AgNWs from the PU fibers.

Finite Element Analysis: To investigate the sensing characteristics of the fiber-based stretchable sensor matrix and their relevant mechanisms, a numerical stress/strain analysis using FEA (COMSOL Multiphysics 5.3) was carried out. A hexahedron PDMS with PU fiber was designed in the actual array size (50 mm [width] × 50 mm [length] × 1 mm [height]). The designed model and the material parameters used for the simulation are listed in Tables S3 and S4, Supporting Information.

Analyses of Strain and Pressure Sensing Characteristics: The electrical conductivity of AgNW-coated PU fiber and C-PDMS was measured by using a resistance-meter and 4 point-probe measurement system, respectively. The relative change in current was measured by using a semiconductor parameter analyzer (Agilent 4156C, Agilent Technologies). The response and relaxation time to each stimulus (strain, pressure, flexion, or temperature) were determined as the minimum time from initial state to target stimulus value using the cyclic loading measurement data. For the dynamic measurement of the sensor matrix, a measuring system comprising a switch mainframe (Keithley 3706A), a dual channel sourcemeter (Keithley 2636B), and a high-speed reed relay MUX card was used, connected to a data acquisition system (DAQ; SnM). Using this measurement system, the acquisition of matrix data from the sensor matrix is possible by sequentially reading the current from each sensor unit (Figure S21, Supporting Information).

Data Preparation and Process for BoW Machine Learning: BoW model is one of the methods for automatically classifying documents based on text. To apply the BoW image classification for the discrimination of intermixed stimuli, image pixel data were generated by normalizing the 10 × 10 matrix current data to 8-bit unsigned bits. In order to apply the generated image pixel data to the BoW model, key features were extracted from the image through the SURF algorithm. After that, K-mean clustering was performed on all of the key features extracted from the plurality of images to remove duplicate or weak key-points. Then, when a new image was input, the feature points of the image were extracted, and the closest feature vector corresponding to each of the extracted key features in the codebook and the SVM was found and classified by applying the category of the feature vector. Experiments were conducted using Matlab R2019a (MathWorks). Also, Statistics and Machine Learning Toolbox and Computer Vision Toolbox were used to carry out the SURF algorithm, K-mean clustering, SVM, and BoW. In this case, for the training sets for machine learning, physical simulation data were used, and for the verifying sets, both simulation data and experimental data were used. The reason to use simulation data for the training sets was to emulate a variety of combinations of intermixed stimuli with larger numbers. However, since the simulation data were obtained using a physical simulation tool, it was expected that the data were very close to the real data sets.

Supporting Information

Supporting Information is available from the Wiley Online Library or from the author.

Acknowledgements

J.H.L. and J.S.H. contributed equally to this work. This research was partially supported by the National Research Foundation of Korea (NRF) grant funded by the Korea government (MSIP) (No. NRF-2019R1A2C2002447), (No. NRF-2019M3F3A1A02071601), and the Institute for Information & Communications Technology Promotion (IITP) grant funded by the Korea government (MSIP) (Grant No. 2017-0-00048,

the Development of Core Technologies for Tactile Input/Output panels in Skintronics (Skin Electronics)).

Conflict of Interest

The authors declare no conflict of interest.

Keywords

cross-reactive sensor matrixes, electronic skin, machine-learning sensors, tactile sensor arrays

Received: February 11, 2020

Revised: March 12, 2020

Published online: April 20, 2020

- [1] J. Y. Oh, S. Rondeau-Gagné, Y. C. Chiu, A. Chortos, F. Lissel, G. J. N. Wang, B. C. Schroeder, T. Kurosawa, J. Lopez, T. Katsumata, J. Xu, C. Zhu, X. Gu, W. G. Bae, Y. Kim, L. Jin, J. W. Chung, J. B. H. Tok, Z. Bao, *Nature* **2016**, 539, 411.
- [2] D. Son, J. Lee, S. Qiao, R. Ghaffari, J. Kim, J. E. Lee, C. Song, S. J. Kim, D. J. Lee, S. W. Jun, S. Yang, M. Park, J. Shin, K. Do, M. Lee, K. Kang, C. S. Hwang, N. Lu, T. Hyeon, D. H. Kim, *Nat. Nanotechnol.* **2014**, 9, 397.
- [3] J. He, P. Xiao, J. Shi, Y. Liang, W. Lu, Y. Chen, W. Wang, P. Théato, S. W. Kuo, T. Chen, *Chem. Mater.* **2018**, 30, 4343.
- [4] X. Tang, T. Zhang, C. Xie, H. Wang, L. Gan, T. Zhou, J. Huang, C. Wu, D. Zeng, *Small* **2019**, 15, 1804559.
- [5] Q. Hua, J. Sun, H. Liu, R. Bao, R. Yu, J. Zhai, C. Pan, Z. L. Wang, *Nat. Commun.* **2018**, 9, 244.
- [6] J. Kim, M. Lee, H. J. Shim, R. Ghaffari, H. R. Cho, D. Son, Y. H. Jung, M. Soh, C. Choi, S. Jung, K. Chu, D. Jeon, S.-T. Lee, J. H. Kim, S. H. Choi, T. Hyeon, D.-H. Kim, *Nat. Commun.* **2014**, 5, 5747.
- [7] T. Someya, Y. Kato, T. Sakurai, T. Sekitani, H. Kawaguchi, S. Iba, *Proc. Natl. Acad. Sci. USA* **2004**, 101, 9966.
- [8] C. Pang, G.-Y. Lee, T. Kim, S. M. Kim, H. N. Kim, S.-H. Ahn, K.-Y. Suh, *Nat. Mater.* **2012**, 11, 795.
- [9] S. Lee, A. Reuveny, J. Reeder, S. Lee, H. Jin, Q. Liu, T. Yokota, T. Sekitani, T. Isoyama, Y. Abe, Z. Suo, T. Someya, *Nat. Nanotechnol.* **2016**, 11, 472.
- [10] M. V. Kovalenko, M. Yarema, P. W. M. Blom, M. A. Loi, F. Cordella, M. Saba, M. Böberl, W. Heiss, D. Jarzab, O. V. Mikhnenko, F. Quochi, A. Gocalinska, G. Hesser, G. Bongiovanni, K. Szendrei, A. Mura, *Adv. Mater.* **2008**, 21, 683.
- [11] W. T. Navaraj, C. G. Núñez, D. Shakhiviel, V. Vinciguerra, F. Labeau, D. H. Gregory, R. Dahiya, *Front. Neurosci.* **2017**, 11, 501.
- [12] Y. J. Yun, W. G. Hong, N. J. Choi, B. H. Kim, Y. Jun, H. K. Lee, *Sci. Rep.* **2015**, 5, 10904.
- [13] X. Xue, Y. Fu, Q. Wang, L. Xing, Y. Zhang, *Adv. Funct. Mater.* **2016**, 26, 3128.
- [14] J. Yun, Y. Lim, G. N. Jang, D. Kim, S. J. Lee, H. Park, S. Y. Hong, G. Lee, G. Zi, J. S. Ha, *Nano Energy* **2016**, 19, 401.
- [15] S. J. Cho, H. Nam, H. Ryu, G. Lim, *Adv. Funct. Mater.* **2013**, 23, 5577.
- [16] G. Wang, B. Wang, S. Han, W. Huang, F. S. Melkonyan, M. J. Bedzyk, X. Zhuang, A. Facchetti, T. J. Marks, J. Yu, L. Zeng, *Adv. Mater.* **2017**, 29, 1701706.
- [17] H. Fang, S. Adjokatse, H. Wei, J. Yang, G. R. Blake, J. Huang, J. Even, M. A. Loi, *Sci. Adv.* **2016**, 2, e1600534.

- [18] J. Chang, A. Legrand, P. Fox, A. Chortos, C. M. Boutry, Z. Bao, Y. Kaizawa, Z. Wang, B. C. Schroeder, *Nat. Electron.* **2018**, *1*, 314.
- [19] K. Shiba, R. Tamura, T. Sugiyama, Y. Kameyama, K. Koda, E. Sakon, K. Minami, H. T. Ngo, G. Imamura, K. Tsuda, G. Yoshikawa, *ACS Sens.* **2018**, *3*, 1592.
- [20] C. H. Park, V. Schroeder, B. J. Kim, T. M. Swager, *ACS Sens.* **2018**, *3*, 2432.
- [21] S. J. Choi, K. H. Ku, B. J. Kim, I. D. Kim, *ACS Sens.* **2016**, *1*, 1124.
- [22] D. Xu, W. Zhu, C. Wang, T. Tian, J. Cui, J. Li, H. Wang, G. Li, *Chem. - Eur. J.* **2014**, *20*, 16620.
- [23] S. J. Oh, J. Choi, J. H. Kim, T. H. Park, B. Park, Y. Cho, C. Kim, H. S. Park, S. Lee, S. C. Jun, H. S. Song, T. H. Ha, D. K. Lee, Y.-S. Ryu, H.-J. Lee, D. H. Woo, Y. M. Jhon, M. Seo, T. Lee, H. Yang, S. H. Kim, J. Oh, H.-S. Kim, *Adv. Mater.* **2018**, *30*, 1706764.
- [24] Y. H. Jung, S. K. Hong, H. S. Wang, J. H. Han, T. X. Pham, H. Park, J. Kim, S. Kang, C. D. Yoo, K. J. Lee, *Adv. Mater.* **2019**, *2019*, 1904020.
- [25] P. Anzenbacher, B. Green, P. Bucek, M. A. Palacios, M. E. Kozelkova, M. E. Kozelkova, *Chem. Soc. Rev.* **2010**, *39*, 3954.
- [26] G. Y. Bae, J. T. Han, G. Lee, S. Lee, S. W. Kim, S. Park, J. Kwon, S. Jung, K. Cho, *Adv. Mater.* **2018**, *30*, 1803388.
- [27] J. H. Low, W. W. Lee, P. M. Khin, N. V. Thakor, S. L. Kukreja, H. L. Ren, C. H. Yeow, *IEEE Rob. Autom. Lett.* **2017**, *2*, 880.
- [28] C. Yu, Y. Zhang, D. Cheng, X. Li, Y. Huang, J. A. Rogers, *Small* **2014**, *10*, 1266.
- [29] T. Q. Trung, S. Ramasundaram, B. U. Hwang, N. E. Lee, *Adv. Mater.* **2016**, *28*, 502.
- [30] W. Tang, T. Yan, J. Ping, J. Wu, Y. Ying, *Adv. Mater. Technol.* **2017**, *2*, 1700021.
- [31] T. Lee, W. Lee, S. W. Kim, J. J. Kim, B. S. Kim, *Adv. Funct. Mater.* **2016**, *26*, 6206.
- [32] S. Park, M. Vosguerichian, Z. Bao, *Nanoscale* **2013**, *5*, 1727.
- [33] N. T. Tien, S. Jeon, D. Kim, T. Q. Trung, M. Jang, B. U. Hwang, K. E. Byun, J. Bae, E. Lee, J. B. H. Tok, Z. Bao, N. E. Lee, J. J. Park, *Adv. Mater.* **2014**, *26*, 796.
- [34] X. Chen, T. Wang, B. K. Chandran, Z. Liu, J. Yu, D. Qi, H. Yang, *Adv. Mater.* **2016**, *28*, 9175.
- [35] S. Gupta, S. Ghosh Mazumdar, *Int. J. Comput. Sci. Manage. Res.* **2012**, *2*, 1578.
- [36] A. Bosch, X. Muñoz, R. Martí, *Image Vis. Comput.* **2007**, *25*, 778.
- [37] V. Vučković, *Rev. Natl. Cent. Digitization* **2008**, *12*, 17.
- [38] H. Bay, A. Ess, T. Tuytelaars, L. Van Gool, *Comput. Vis. Image Underst.* **2008**, *110*, 346.
- [39] X. Niu, S. Peng, L. Liu, W. Wen, P. Sheng, *Adv. Mater.* **2007**, *19*, 2682.
- [40] D. Hu, T. K. Cheng, K. Xie, R. H. W. Lam, *Sensors* **2015**, *15*, 26906.